Heliyon 9 (2023) e23106

Contents lists available at ScienceDirect

Heliyon

journal homepage: www.cell.com/heliyon

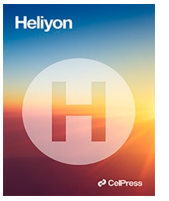

Integrated synthesis and comprehensive characterization of TiO2/AgBi2S3 ternary thin films via SILAR method

Sachin Padwal [a,*], Rahul Wagh [b], Jivan Thakare [c], Rajendra Patil [d]

[a] Science Department, Government Polytechnic Nashik, New Building Campus, Samangaon Road, Nashik Road, Nashik, 422101, Maharashtra, India
[b] Department of Physics, PSGVP Mandal's Arts Commerce & Science College, Shahada, Nandurbar, 425409, Maharashtra, India
[c] Principal Research Engineer, Electrochemical Process Development, Energy and Environmental Research Center, Grand Forks, ND, 58202-9018, USA
[d] Department of Physics, PSGVP Mandal's Arts Commerce & Science College, Shahada, Nandurbar, 425409, Maharashtra, India

ARTICLE INFO

Keywords:
Ternary metal chalcogenide
SILAR
AgBi2S3
UV visible spectroscopy
Optical energy band gap
Electrochemical impedance spectroscopy
Photoelectrochemical

ABSTRACT

$AgBi_2S_3$, a copious and innocuous ternary metal chalcogenide affiliated with the I-V-IV group of semiconductors, was synthesized. With an energy gap of 1.2eV, it closely matches the optimal 1.39eV for solar cell absorbers. Importantly, this chalcogenide exhibits a high absorption coefficient of 10^5 cm^{-1} at 600 nm. Using the successive ionic layer adsorption and reaction (SILAR) method; we deposited an $AgBi_2S_3$ thin film onto a titanium dioxide (TiO_2) thin film. Characterization techniques encompassed XRD, SEM, EDXS, UV–Vis, EIS, and PEC performance analyses. The resulting $TiO_2/AgBi_2S_3$ composite film ranged in thickness from 8 μm to 13 μm, with particle sizes spanning 20 nm–265 nm. Notably, the deposition of $AgBi_2S_3$ onto the TiO_2 film caused depreciation in the TiO_2 energy gap from 3.1eV to 1.7eV. Furthermore, it significantly enhanced the TiO_2 film's absorbance across the visible and near-infrared regions. Intriguingly, the $TiO_2/AgBi_2S_3$ composite film also exhibited discernible photoelectrochemical behavior.

1. Introduction

With the advancement in the field of science and technology the energy requirement of humans on the globe is escalating day by day. According to the International Energy Agency (IEA) report published in November 2021, world's total energy requirement for the year 2021 was about 168 000 Terawatt-hours [1]. In its report IEA has predicted increase in energy will continue in coming years especially from developing countries. As per the breakdown of energy produced by different sources the overall energy produced using fossil fuel is 74 500 Terawatt-hours according to the IEA report published in 2020 [2]. Consumption of fossil fuels not only degrades environment but also prime reason for greenhouse gas emissions and climate change across entire world [3]. As per the reports of IEA published in 2019 the total amount of solar energy that reach the outer atmosphere is about 164 W/m^2. On a clear sunny day when the sun is exactly overhead, the amount of solar radiation reaching earth can attain maximum value of 1000 W/m^2 [4]. The amount of solar radiation reaching earth is influenced by time of day, weather conditions and latitude. Thus, solar energy is most easily available source of energy, available in most parts of the earth throughout the year. Hence, it can be supposed as an alternative to fossil fuels.

Solar cells based on silicon are successfully used to yield power accomplished with almost zero environmental emissions. However,

* Corresponding author. Department of Physics, PSGVP Mandal's Arts Commerce & Science College, Shahada, Nandurbar, 425409, Maharashtra, India.
E-mail address: sachin3380@gmail.com (S. Padwal).

https://doi.org/10.1016/j.heliyon.2023.e23106
Received 19 September 2023; Received in revised form 20 November 2023; Accepted 27 November 2023
Available online 2 December 2023

these silicon based solar cells have higher fabrication cost and lower efficiency as compared with fossil fuels [5]. Regan & Gratzel in 1991 fabricated first dye sensitized solar cell (DSSC) [6]. A DSSC is solar cell which is fabricated using variety of materials and low cost methods. The primary component of a DSSC is a very lithe layer of titanium dioxide (TiO_2) deposited with another lithe film layer of organic or inorganic material more commonly named as dye molecule [6,7]. TiO_2 due to its non-toxic and high conversion efficiency is preferred choice for DSSC [8]. A proficient sensitizer having optimum light absorption in visible spectrum and near infra-red region can best suit as absorber layer for DSSC [9]. Many semiconducting materials such as cadmium selenide, cadmium sulfide, lead sulfide, and antimony sulfide have been used as a sensitizer for DSSC. All of these chemical compounds are binary metal chalcogenide, and similarly, ternary metal chalcogenide are also useful as dye for the DSSC [10]. A TiO2–Ag–Ag2S nanojunction biosensor was developed for specific and sensitive detection of CD44 protein, offering potential for breast cancer diagnosis. The biosensors unique structure and Z-scheme heterojunction enable stable photocurrent output and a wide detection range [11]. Hybrid AgInS2–TiO2 nanoarchitectures exhibit enhanced visible light photocatalysis, achieving efficient pollutant degradation and H2 generation [12]. Ternary metal chalcogenide are very less investigated as dye molecule in DSSC since they are difficult to synthesize.

Silver bismuth sulfide (AgBi2S3) is associated with the I-V-VI set of semiconducting materials and is a benign compound. AgBi2S3 have energy gap of 1.2 electron volt which is nearly akin to the ideal energy gap of 1.39 electron volt for absorbers layer of solar cell. Apart from this it also have good absorption coefficient of 10^5 $(cm)^{-1}$ at $\lambda = 600$ nm. AgBi2S3 exhibits a predominant tetragonal crystal structure as resoluted by X-ray diffraction analysis. This crystalline arrangement conforms to the I-42m space group, indicating specific symmetry properties. The crystal lattice comprises alternating layers of edge-sharing AgS_6 octahedral and BiS_6 octahedral, interconnected by bridging sulfide ions. It is noteworthy that AgBi2S3 manifests polymorphism, displaying multiple crystallographic phases, each characterized by unique electronic and optical characteristics. AgBi2S3 hold great promise in various scientific and technological domains, including photovoltaics, thermoelectric materials, optoelectronics, and catalysis. This compounds tunable properties, such as band gap and electrical conductivity, make it ideal candidates for emerging applications, ranging from solar cells to quantum-dot-based technologies. Huang et al. reported the deposition of AgBiS2 by the two-stage SILAR method [13]. Shuqin Zhou et al. reported electrochemical atomic deposition of AgBi2S3 on a rutile TiO2 layer [14]. They have reported a transposition efficiency of 0.950 %. The synthesis of sole molecular precursor solution for a silver bismuth sulfide thin film produced through the blending of existing metal nitrates and thiourea within a solvent medium of dimethyl sulfoxide (DMSO) was reported by Ening Gu et al. [15]. A N Rodriguez et al. reported chemical deposition of Bi2S3/Ag2S thin film with optical band gap energy of 0.96–1.36 eV and electrical conductivity of (10^{-5} to 10^{-2}) $(\Omega\ cm)^{-1}$ [16]. Biljana Pejova et al. fabricated a three-dimensional assembly of densely packed quantum dots (QDs) composed of silver bismuth sulfide within thin film structures. Sonochemically with optical band gap energy of 1.40 eV [17]. Narendra Pai et al. applied silver bismuth sulfide via the technique of spray pyrolysis for deposition having thickness (60.0–70.0) nm for solar energy application and exhibited an efficiency of 1.50 % [18]. Maria Bernechea et al. showcased a low-temperature hot injection synthesis method to produce silver bismuth sulfide, intended for application in solar cells, achieving a conversion efficiency of 6.3 % [19]. The present study presents a successful synthesis of ternary metal chalcogenide, silver bismuth sulfide (AgBi2S3), utilizing the innovative SILAR method, which has not been previously documented in the literature. Prior to the AgBi2S3 synthesis, a titanium dioxide (TiO2) thin film was deposited onto a glass/FTO substrate via the sol-gel spin-coating technique, employing commercially available TiO2 powder as the precursor material. Subsequently, the TiO2 thin film was sensitized with an AgBi2S3 thin film using the SILAR technique. The SILAR technique for thin-film synthesis and deposition is characterized by its simplicity, versatility, and cost-effectiveness. It offers distinct advantages, including layer-by-layer growth, low-temperature deposition, minimal equipment requirements, and the ability to achieve conformal coatings. Noteworthy benefits of the SILAR method encompass precise control over film thickness and composition, uniformity across the substrate, scalability for various applications, and compatibility with diverse substrate materials. Consequently, SILAR holds significant value for both research endeavors and industrial applications across a wide spectrum of disciplines. Our research involves the fabrication of a TiO2 thin film sensitized with AgBi2S3 thin film, followed by thorough characterization of the material using advanced characterization methods.

2. Experimental section

2.1. Deposition of thin film of titanium dioxide (TiO_2) by spin coating technique

To achieve precise deposition of a TiO2 thin film upon a fluorine doped tin oxide (FTO) glass substrate, a meticulous sol-gel process was employed. This involved selecting high-purity (99.9 %) TiO2 powder with 25 nm particles. The sol-gel solution was carefully balanced, incorporating 10 ml of 70 % ethanol to disperse TiO2 nanoparticles uniformly, 2 ml of 98 % acetyl acetone to control hydrolysis, and 1 ml of nitric acid (69–71 %) to adjust pH and catalyze the sol-gel reaction. These components were stirred for 15 h to ensure a well-dispersed sol. The TiO2 thin film was embedded on an FTO substrate employing spin coating. The FTO glass underwent rigorous cleaning to remove potential contaminants. The sol-gel was evenly applied over the substrate and gyrated at 900 rpm for 1 min at room temperature, resulting in a uniform thin film. To enhance the films crystalline attributes, it was annealed inside a muffle furnace at 400 °C with a controlled heating rate to minimize thermal shock. The post-annealed film exhibited robust adhesion to the FTO substrate, attributed to tailored processing conditions. These precise steps led to the creation of a high-quality TiO2 thin film ready for further analysis and characterization.

2.2. Deposition of thin film of ternary compound silver bismuth sulfide ($AgBi_2S_3$) by SILAR method

In the pursuit of fabricating a robust composite system comprising $AgBi_2S_3$ thin films deposited onto n-type wide band gap

semiconducting TiO_2 thin films, a judiciously designed SILAR methodology was employed. The amalgamation of three distinct precursor solutions was strategically orchestrated to culminate in the desired $AgBi_2S_3$ thin film deposition. Leveraging the fundamental principles of SILAR, this process involved the controlled introduction of specific precursor ions onto the TiO_2 thin film-coated FTO substrate, resulting in a well-ordered and precisely engineered thin film composite. The SILAR sequence entailed a meticulous choreography of discrete steps, each contributing to the incremental buildup of the $AgBi_2S_3$ thin film structure. This intricate dance commenced with the immersion of the TiO_2 thin film-coated FTO substrate into a 0.1 M $AgNO_3$ solution (pH~9-10 adjusted by adding few drops of liquid ammonia and aqueous viscosity) for 20 s, where the Ag^{+1} ion from the silver nitrate served as a potent oxidizing agent. Subsequent to this immersion, a judicious rinsing in distilled water for 10 s ensued, ensuring the controlled removal of any residual Ag^{+1} ion. The process continued its rhythmic progression with the introduction of the Bi^{+3} ions, derived from the 0.1 M Bi $(NO_3)_3.5H_2O$ (pH~8–9 with low to medium viscosity~1 to 1.5 cP) precursor solution for 20 s. The incorporation of $Bi(NO_3)_3.5H_2O$ marked a pivotal step in the SILAR cycle, fostering the controlled reaction necessary for the growth of the $AgBi_2S_3$ thin film. An intermediate rinsing phase again followed, meticulously separating the distinct phases of the cycle. The crescendo of this orchestrated symphony unfolded with the infusion of S^{-2} ions. The 0.1 M CH_3CSNH_2 solution(pH~7–8 and aqueous viscosity), rich in thioacetamide, played a dual role. It not only contributed the sulfur ions required for the $AgBi_2S_3$ formation, but also acted as a reducing emissary, inducing the diminution of the precursor ions introduced in the earlier stages of the SILAR cycle. This redox chemistry ushered in the formation of elemental silver, bismuth sulfide, and byproducts including disulfide and acetamide species. Concurrently, the liberation of nitric acid as a byproduct of the oxidation process underscored the dynamic intricacies of the chemical transformations at play. Fig. 1(a) illustrates the schematic depiction outlining the SILAR technique employed in the fabrication process of thin films.

The completion of a SILAR cycle was punctuated by a meticulously orchestrated sequence of rinsing steps, each aimed at purifying

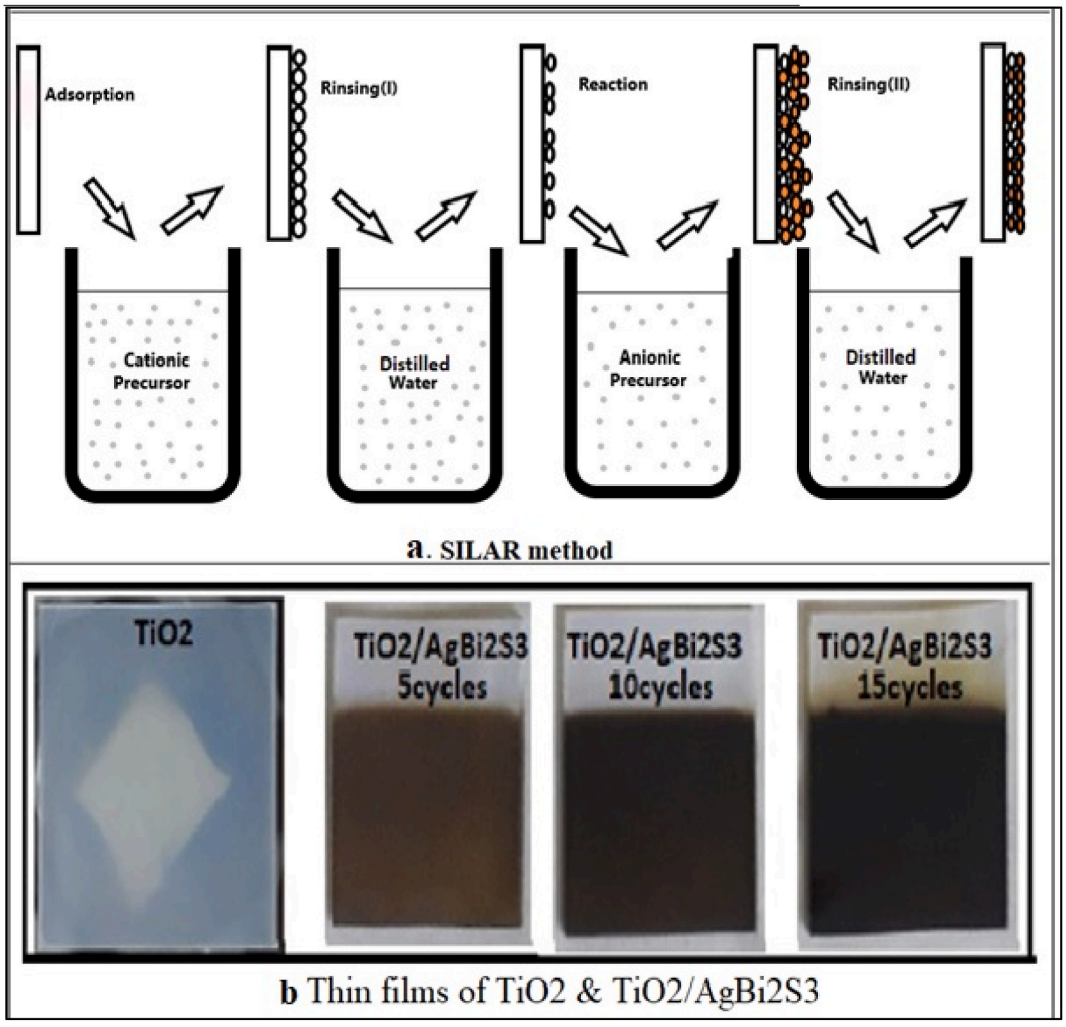

Fig. 1. Schematic diagram for a) SILAR method for thin film deposition and b) thin films of TiO_2 by spin coating & $TiO_2/AgBi_2S_3$ for 5, 10 & 15 SILAR cycles respectively.

and preparing the evolving thin film structure for the subsequent cycle. This iterative process, characterized by its choreographed sequence of ion adsorption and chemical reaction steps, ultimately culminated in the progressive deposition of the $AgBi_2S_3$ thin film. The evolution of the deposited thin film's characteristics was tracked through a series of SILAR cycles, yielding insights into the growth dynamics and the consequential transformation in film thickness. Remarkably, the progressive increase in the number of cycles translated into a visually discernible transition from a pale light brown hue to a deeper shade of brown. This optical manifestation served as a visual testament to the gradual accumulation of the $AgBi_2S_3$ thin film material, elucidating the synergistic interplay between the deposition process and the evolving film architecture. By manipulating the number of SILAR cycles, composite films of TiO_2/$AgBi_2S_3$ were systematically engineered, each characterized by a controlled and tunable thickness. The judicious orchestration of this multifaceted process yielded composite films that held promise for diverse applications, underlining the inherent power of the SILAR methodology in designing intricate thin film architectures. These insights contribute to the expanding repertoire of advanced materials synthesis techniques and pave the way for future explorations in tailoring composite thin films for a spectrum of technological pursuits. The schematic representation of SILAR method for deposition of thin films along with TiO_2/$AgBi_2S_3$ composite thin film for 5, 10 & 15 cycles of SILAR is shown in Fig. 1(b and c).

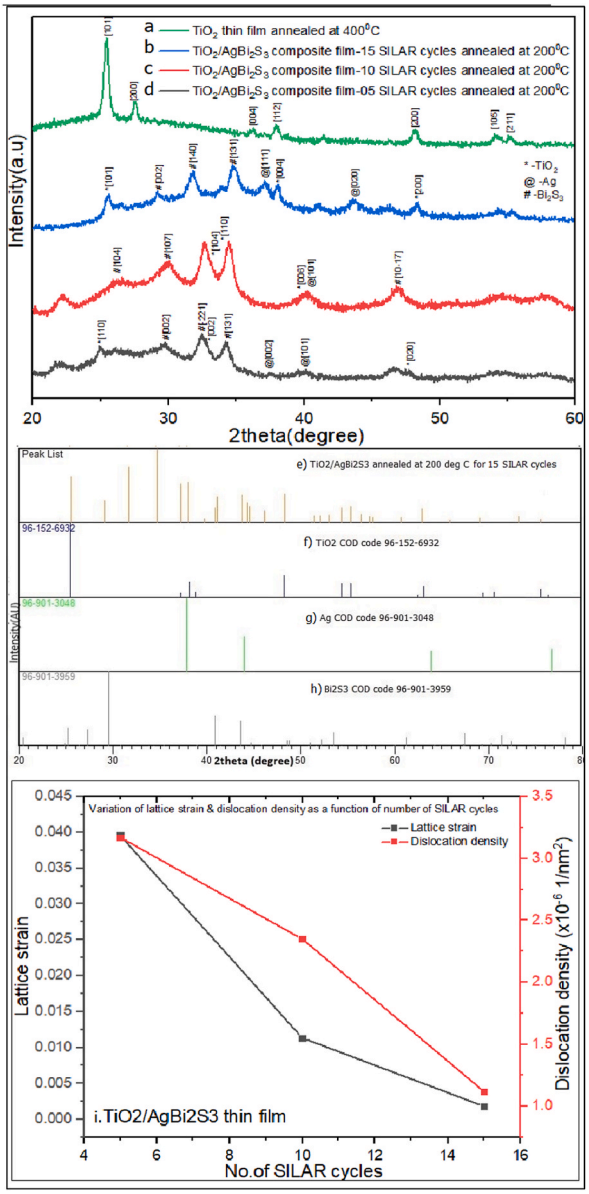

Fig. 2. XRD pattern for a) TiO2 thin film annealed at 400 °C, b-c-d) TiO2/AgBi2S3 composite film for 05, 10 & 15 SILAR cycles, e) TiO2/AgBi2S3 composite film for 05 SILAR cycles, f-g-h) Matched reference COD for TiO2 (96-152-6932), Ag (96-901-3048) & Bi2S3 (96-901-3959), i) Variation of lattice strain & dislocation density as a function of number of SILAR cycles for TiO2/AgBi2S3 composite film.

The composite film TiO2/AgBi2S3 was then annealed at 200° degree C for 30 min to enhance its crystallinity in muffle furnace. The temperature of 200 °C was achieved with the rate of 50 °C per 15 min. Post annealing the film was cooled down to room temperature with course of time. It is expected that the enhanced crystallinity resulting from annealing will lead to improved optical and electrochemical properties of the composite film. The annealing process may facilitate the reduction of defects and disordered regions, resulting in increased charge carrier mobility and enhanced light absorption.

3. Characterization technique

The structural analysis of the TiO2/AgBi2S3 composite thin film was conducted via X-ray diffractometry utilizing an automated Bruker D8 advanced X-ray diffractometer, scanning a diffraction angle range of 20° to 80°. The film's average crystallite size was determined employing the Scherrer formula. Optical absorption characteristics were investigated using a Jasco UV–Visible spectrophotometer (V 630) across wavelengths ranging from 200 nm to 800 nm at room temperature. The optical bandgap energy was derived from the Tauc plot correlating ($h\nu$) against $(\alpha h\nu)^2$. Surface topography and cross-sectional analysis were performed using a scanning electron microscope (SEM) equipped with an energy dispersive spectrometer (EDS) detector (Quanta 200 ESEM, Netherlands). Electrochemical impedance spectroscopy (EIS) was carried out using a potentiostat/galvanostat (IVIUM Vertex model). The photoelectrochemical (PEC) performance was evaluated utilizing a 3A steady state solar simulator SS-F5-3A (Enli Technology Co., Taiwan). Contact angle measurements were executed through a custom-built setup employing a high-definition 16-megapixel Sony IMX471 camera.

4. Results and discussion

4.1. Structural analysis

The structural elucidation of the TiO2 thin film and composite film, comprising $TiO_2/AgBi_2S_3$, was undertaken through X-ray diffraction (XRD) analysis, a powerful strategy employed for determining the crystalline attributes of a given sample. In the quest to probe the intricate structural properties of the composite, XRD characterization was meticulously executed, yielding the XRD pattern depicted in Fig. 2(a–d). A comprehensive examination of this pattern reveals a discernible interplay of three distinct components: TiO_2, Ag, and Bi_2S_3. The XRD peaks linked with TiO_2 were meticulously matched with the reference COD code 96-152-6932, affirming the presence of the anatase phase accompanied by a tetragonal crystal system of TiO2 (space-group = I 41/a m d; space-group number = I 41; lattice parameter a, b & c = 3.7710, 3.7710 & 9.4300 A^0 respectively; calculated density = 3.96 g/cm^3; volume of cell = 134.10 10^6 p.m.^{3}; RIR = 5.2). As the number of SILAR cycles for deposition of AgBi2S3 were increased from 5 to 15 the crystal structure of TiO2 changed from tetragonal to cubic and finally settled as monoclinic. The observed change in the crystal structure of TiO2, transitioning from tetragonal to cubic and ultimately settling into a monoclinic phase as the number of SILAR cycles for AgBi2S3 deposition increases, strongly implies a significant interaction or influence between the deposited AgBi2S3 and the TiO2 substrate. For 15 cycles the zenith of peak intensity manifests itself at a 2θ value of 24.418°, attributed to diffraction from the [101] plane as seen in Fig. 2(f). Further, notable peaks at 2θ values of 48.226° and 38.143°, corresponding respectively to the [200] and [004] diffraction planes, substantiate the crystalline nature of the TiO_2 phase, as illustrated in Fig. 2 (c). Within the Ag component, the XRD pattern seamlessly aligns with the reference COD code 96-901-3048, indicative of a cubic crystal system for Ag (space-group = F m −3 m; space-group number = 225; lattice parameter a, b & c = 4.1170, 4.1170 & 4.1170 A^0 respectively; calculated density = 10.27 g/cm^3; volume of cell = 69.78 10^6 p.m.^{3}; RIR = 18.68). In case of Ag the crystal structure changed from cubic to hexagonal as the SILAR cycles were enhanced from 5 to 15. Remarkably for 15 cycles, the pinnacle of peak intensity emerges at a 2θ value of 37.819°, attributed to diffraction from the [111] plane as seen in Fig. 2(g). Complementary peaks, situated at 2θ values of 43.95° and 76.712°, corresponding respectively to the [020] and [131] diffraction planes, further accentuate the crystallinity of the Ag phase, as exemplified in Fig. 2 (d). In the realm of Bi_2S_3, the observed XRD peaks exhibit a concordance with the reference COD code 96-901-3959, emblematic of a hexagonal crystal system for Bi2S3 (space group = R −3 m; space group number = 166; lattice parameter a, b & c = 4.1500, 4.1500 & 39.1900 A^0 respectively; calculated density = 7.94 g/cm^3; volume of cell = 584.52 10^6 p.m.^{3}; RIR = 17.51). The crystal structure of Bi2S3 changed from hexagonal to orthorhombic as the SILAR cycles were raised from 5 to 15. Predominantly, the most intense peak materializes at a 2θ value of 29.511°, attributed to diffraction from the [107] plane for 15 cycles as shown in Fig. 2(h). Additional substantial peaks, positioned at 2θ values of 40.828° and 43.583°, pertaining respectively to the [10–14] and [110] diffraction planes, further underscore the crystalline nature of the Bi_2S_3 phase, as visualized in Fig. 2 (e). The change in the crystal structure of Ag and Bi2S3 during SILAR deposition from 5 to 15 cycles is likely due to factors such as increased film thickness, nucleation and growth effects, kinetics, thermodynamics, surface interactions, phase transformations, stress and strain, and deposition rate variations. The XRD pattern of the standard reference COD for TiO2, Ag, and Bi2S3 matches with the pattern of the TiO2/AgBi2S3 composite film, thereby confirming the synthesis of the ternary compound.

The XRD analysis unfolds a distinctive revelation concerning the ternary metal chalcogenide, $AgBi_2S_3$, unearthing a captivating interplay of three diverse crystal structures: tetragonal, cubic, and hexagonal. This intriguing observation intimates the coexistence of discrete crystal phases within the confines of the chalcogenide material, suggesting the intriguing prospects of phase separation or crystallographic heterogeneity within this ternary composition. The presence of such divergent crystal structures bestows consequential ramifications upon the material's inherent properties, thus engendering an avenue of exploration that reverberates across a plethora of scientific inquiries. The manifestation of distinct crystal phases may find its genesis in a multitude of contributing factors, encompassing synthesis conditions, intricate growth kinetics, and the nuanced influence of post-treatment procedures. This meticulous

XRD analysis serves as a substantiating testament to the successful synthesis of a polycrystalline $AgBi_2S_3$ ternary metal chalcogenide thin film. The genesis of this achievement is rooted in the elegant utilization of the SILAR, meticulously enacted upon a wide band gap n-type semiconducting TiO_2 thin film substrate. The profound insights gleaned from this XRD analysis stand poised to propel our understanding of material synthesis and crystalline behavior within composite systems, laying the foundation for myriad scientific advancements. The mean crystallite size (D) of composite thin film of $TiO_2/AgBi_2S_3$ was determined using Scherrer equation (1) [20],

$$D = \frac{0.9\,\lambda}{\beta \cos\theta} \tag{1}$$

In this equation, λ represents the X-ray wavelength (specifically, CuKα radiation with a value of 0.154 nm), while θ denotes the Bragg diffraction angle. Additionally, β signifies the full width half maximum of the X-ray diffraction peaks observed at various θ angles. Specifically, as the number of SILAR cycles increased to 05, 10, and 15, the calculated average crystalline sizes correspondingly reached 56.0 nm, 62.5 nm, and 94.5 nm, respectively. Williamson Hall plot method was also utilized to estimate average crystalline sizes of same composite thin film [21]. The values calculated as 19.2 nm, 25.09 nm & 59.27 nm respectively for 5, 10 & 15 SILAR cycles. The differences in the average values are because of differences in assumptions and methodologies of these two approaches. The discernible augmentation in crystallite size ascribed to the escalating number of SILAR cycles unveils an insightful trend. Evidently, the deposition process exerts a profound influence on the nucleation and growth dynamics of the crystallites within the composite. The iterative nature of SILAR, involving the deposition of successive layers, inherently provides enhanced opportunities for the crystalline entities to evolve. This iterative regime catalyzes the augmentation of the crystallites' dimensions, leading to the observed enlargement in average size. The observed dependence of crystalline size on the number of SILAR cycles underscores a compelling relationship between the intricate growth kinetics and the overarching deposition process. The interplay between the rate of crystal growth during each SILAR cycle and the cumulative impact of layer-by-layer deposition over multiple cycles intricately governs the final dimensions of the crystalline entities. This intricate nexus between growth kinetics and deposition process dynamics forms a pivotal facet of the evolving composite thin film architecture. The resultant crystallite sizes serve as tangible indicators, unveiling the intricate interplay of deposition conditions and growth kinetics in sculpting the final structural attributes. The comprehensive XRD analysis thus substantiates the pivotal role of the SILAR methodology in engineering the crystalline architecture of the $TiO_2/AgBi_2S_3$ composite thin film, shedding light on the nuanced relationships that underscore its growth and evolution. As the SILAR cycles increase (from 5 to 15 cycles), the crystallite size of the composite film also increases. Larger crystallites may affect the material's ability to absorb light and modify its optical properties. In this case, the increase in crystallite size may contribute to the reduction in the optical energy band gap, making the material more absorbent.

The assessment of lattice strain, a vital indicator of the structural response of solid materials to external forces or stressors, stands central to our characterization of the TiO2/AgBi2S3 composite thin film through X-ray diffraction (XRD) analysis. The manifestation of lattice strain is indicative of the deformation incurred within the crystal lattice of the material. To quantitatively elucidate this phenomenon, we calculated the average lattice strain percentage (ε) and dislocation density (δ) of the post-annealed TiO2/AgBi2S3 composite film employing equations (2) and (3) [22]. In the context of sensitizing semiconductors with dye molecules, it becomes essential to discern the origins of strain generation within the composite system. This strain may arise from intricate interactions between the AgBi2S3 dye molecule and the underlying TiO2 semiconductor, thereby influencing the lattice parameters and structural attributes. Moreover, the very deposition technique itself may inherently contribute to the strain observed within the composite thin film. As we delve deeper into the complex interplay between the constituents, the origins of lattice strain in the TiO2/AgBi2S3 composite film unveil a multifaceted tapestry of factors, including deposition dynamics, molecular interactions, and underlying crystallographic properties. The quantification and understanding of these strain-induced phenomena hold the key to unlocking a deeper comprehension of the composite's behavior, ultimately paving the way for optimized performance in various application domains.

$$\varepsilon = \frac{\beta}{4\tan\theta} \tag{2}$$

$$\delta = \frac{1}{D^2} \tag{3}$$

Where D is average crystallite size. The evaluation of lattice strain, a pivotal parameter characterizing the deformation within the crystal lattice of a solid material, was meticulously conducted across varying SILAR cycle numbers—namely, 5, 10, and 15. The computed average lattice strain values of 0.319×10^{-3}, 0.256×10^{-3}, and 0.112×10^{-3}, correspondingly, unveil an intricate interplay between the deposition process and resultant crystalline structure. The discernible alterations in lattice strain inherently mirror the subtle adjustments in the crystalline arrangement of the composite thin film. The diverse SILAR cycle numbers engender distinctive degrees of lattice distortion or relaxation, inherently influencing the material's structural attributes and subsequent properties. The lattice strain decreases as the SILAR cycles increase. Reduced lattice strain can affect the material's electronic band structure, potentially leading to a change in its optical properties. The decrease in strain may contribute to the observed reduction in the optical energy band gap. Concomitantly, the meticulous computation of dislocation density across the same range of SILAR cycles yielded quantifiable insights. The dislocation density values of $3.17 \times 10^{-6,}$ 2.348×10^{-6}, and 1.119×10^{-6} $1/nm^2$ for SILAR cycles of 5, 10, and 15, respectively, unveil an intriguing trend. The diminishing dislocation density with increasing SILAR cycles serves as a tangible manifestation of a notable reduction in crystal defects and dislocations. This pronounced decline corroborates the notion that as

additional layers are deposited through successive cycles, the crystalline imperfections within the material are substantially ameliorated. Intriguingly, the observed correlation between dislocation density and SILAR cycle number underscores the underlying dynamics of crystal nucleation and growth. The dislocation density decreases with an increase in SILAR cycles. A lower dislocation density can lead to improved crystal quality and fewer defects, which may enhance the material's optical properties, such as better light absorption and a reduced band gap. Enhanced SILAR cycles bestow a favorable milieu for the meticulous evolution of crystalline entities, accentuating the conditions conducive to minimal crystal imperfections. The conspicuous diminution in dislocation density, and correspondingly, the attainment of petite values, ultimately signifies the commendable crystallinity encapsulated within the thin film [23]. This refined understanding of lattice strain and dislocation density, obtained through meticulous XRD analysis and computation, contributes to an enriched comprehension of the evolving composite's structural attributes. These insights, encompassing the intricate interplay of SILAR cycles and their profound impact on the material's crystalline architecture, underpin the foundation for material design and optimization strategies.

3.2. Morphological analysis

Surface morphological investigation of both the pristine TiO2 and the TiO2/AgBi2S3 composite films was meticulously conducted via scanning electron microscopy (SEM), as illustrated in Fig. 3. In Fig. 3(a), the SEM micrograph depicting the surface morphology of the TiO2 thin film unveils a distribution of nanoparticles (with a particle size of 25 nm, sourced from Degussa Germany) uniformly dispersed across the entirety of the substrate. Remarkably, these nanoparticles display a seamless spatial arrangement, devoid of direct interactions with the fluorine-doped tin oxide (FTO) substrate. This judicious design ensures an impervious and stable interface between the TiO2 layer and the FTO substrate, thus promoting the unhindered transfer of charge and preventing any potential interfacial perturbations. The conspicuous absence of cracks or defects within the TiO2 thin film engenders a robust platform for enhanced electrolyte diffusion and charge transmission [24]. This continuous, defect-free morphology fosters an expedited interaction between the film and the electrolyte, facilitating improved charge transport and leading to an elevated performance profile. The assessment of the TiO2 thin film reveals an average thickness of approximately 7.26 μm, characterized by a standard deviation of 0.188 μm as seen in Fig. 3(e). This uniformity in film thickness substantiates an equitable light absorption throughout the substrate, synergistically enhancing charge transport efficacy, device efficiency, and overall stability.

The SEM micrographs in Fig. 3(b), (c), and 3(d) delineate the evolving surface morphology of the TiO2/AgBi2S3 composite film for varying SILAR cycle numbers—namely, 5, 10, and 15. With increasing SILAR cycles, a discernible transformation is evident, where the AgBi2S3 nanoparticles tend to aggregate, consequently augmenting their particle size. Intriguingly, these AgBi2S3 nanoparticles showcase an interconnected architecture, entailing an intricate web-like structure. This interlinked nanoparticle arrangement intimates a pronounced interparticle interaction, exerting a pivotal influence on the material's charge conductivity, transport characteristics, and overall performance attributes. The SEM micrograph further reveals the presence of micro cracks within the AgBi2S3 thin film, conferring a unique avenue for improved electrolyte permeation and facilitated electron transport. Furthermore, the film thickness of the AgBi2S3 component expands in tandem with increasing SILAR cycle numbers. This expansion is particularly notable, evolving from approximately 1 μm–3 μm and subsequently to 5 μm as the SILAR cycles ascend from 5 to 15. Importantly, this augmentation in AgBi2S3 thin film thickness remains consistent and uniform throughout the entire length of the substrate within each individual SILAR cycle, as succinctly captured in Fig. 3(f), (g), and 3(h). The conglomeration of nanoparticles, the interlinked particle structure, the presence of micro cracks, and the expanding film thickness collectively wield a substantial influence on the performance landscape of the TiO2/AgBi2S3 composite thin film. These characteristics exercise pivotal roles in shaping light absorption dynamics, guiding charge carrier transport pathways, and, crucially, impacting the composite's overall efficiency and stability. The

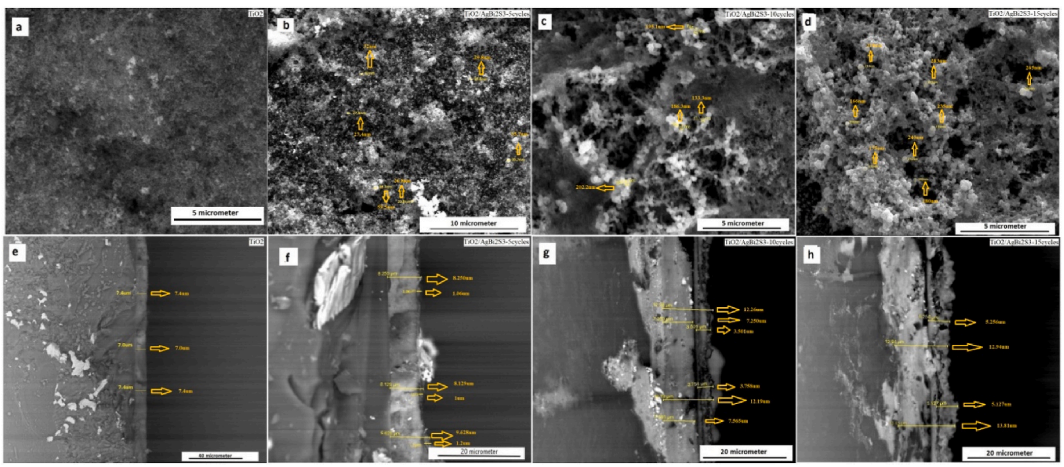

Fig. 3. SEM surface micrograph of a) TiO_2 thin film, b-c-d) $TiO_2/AgBi_2S_3$ composite film for 5, 10 & 15 SILAR cycles respectively. Cross section micrograph of e) TiO_2 thin film and f-g-h) $TiO_2/AgBi_2S_3$ composite film for 5, 10 & 15 SILAR cycles respectively.

comprehensive SEM analysis encapsulates these intricate features, casting illuminating insights into the morphological evolution and the ensuing implications for the composite's multifaceted functionality.

The particle size characterization of the AgBi2S3 thin film for varying SILAR cycles (5, 10, and 15) has been meticulously examined, revealing insightful trends, as depicted in the particle size histogram illustrated in Fig. 4(a-b-c). Comprehensive details regarding the synthesized average particle sizes are succinctly documented within the table featured in Fig. 4(h), thereby providing a comprehensive overview of the observed variations. A notable evolution in particle size characteristics is unveiled as the SILAR cycles escalate from 5 to 10. The minimum and mean particle sizes undergo substantial elevation within this cycle range. Particularly intriguing is the observation of a distinct particle size histogram profile: a narrower distribution emerges for 5 cycles, while progressively broader and more uniformly distributed histograms manifest for 10 and 15 cycles. This nuanced evolution of particle size distribution is instrumental in deciphering the underlying growth dynamics and the consequential morphological attributes of the composite films. The surface morphology is further illuminated through three-dimensional surface plots, as depicted in Fig. 4(g-*d*-e-f). The topographical intricacies of the FTO substrate, obscured by the deposition of titanium dioxide nanoparticles in the case of the TiO2 thin film, and the concurrent overlay of silver bismuth sulfide nanoparticles in the TiO2/AgBi2S3 composite film, are strikingly apparent. Notably, the uniformity of the pattern, comprising gorges and ridges, is accentuated with increasing SILAR cycles. The elevation of gorges and the depth of ridges intensify in tandem with the augmentation of cycle numbers. This discernible uniformity underscores the shielding effect of the FTO substrate against direct exposure, as astutely highlighted in Fig. 4(d-e-f-g). The discernible mesoporous texture, inherent across all films within various SILAR cycles, further substantiates the comprehensive characterization. The evolving film thickness is perceptible from the topographical profiles in Fig. 4(d-e-f-g), underscoring the intricate influence of the deposition process and cycle numbers on the surface features. This dynamic interplay has far-reaching implications for the optical properties of the films, encompassing light scattering phenomena and charge transport dynamics. Insights gleaned from the standard deviation values enumerated within the table presented in Fig. 4(h) further augment our understanding of the particle size distribution. For 5 SILAR cycles, the deposition process and conditions converge to yield a population of particles characterized by a notably uniform size

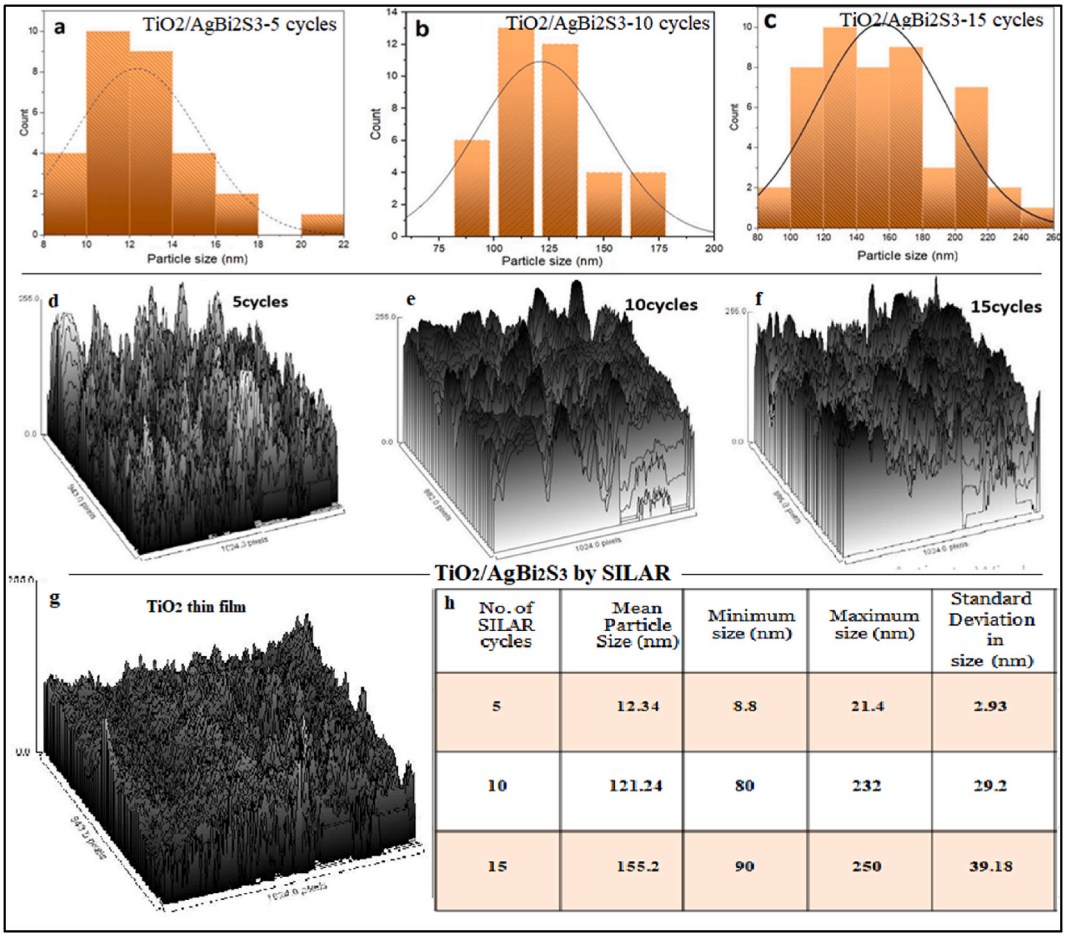

h

No. of SILAR cycles	Mean Particle Size (nm)	Minimum size (nm)	Maximum size (nm)	Standard Deviation in size (nm)
5	12.34	8.8	21.4	2.93
10	121.24	80	232	29.2
15	155.2	90	250	39.18

Fig. 4. a-b-c) Average particle size histogram for $TiO_2/AgBi_2S_3$, composite thin film for 5, 10 & 15 SILAR cycles respectively, d-e-f) 3D surface plot for $TiO_2/AgBi_2S_3$, composite thin film for 5, 10 & 15 SILAR cycles respectively g) 3D surface plot of TiO_2 thin film deposited by spin coating method & h) Summary of particle size details for $TiO_2/AgBi_2S_3$, composite thin film for 5, 10 & 15 SILAR cycles.

distribution. In contrast, the standard deviation values corresponding to 10 and 15 SILAR cycles suggest a broader range of particle sizes within the films. This diversification potentially stems from intricate variations in growth conditions, nucleation processes, or other intricate factors inherent to the deposition process. This distinct dichotomy of particle size distribution carries profound implications. A narrower size distribution inherently fosters enhanced uniformity, a vital trait that can yield more consistent and predictable material properties. These encompass critical facets such as light absorption dynamics, charge transport kinetics, and surface interactions. Conversely, a broader size distribution introduces an element of heterogeneity, thereby potentially giving rise to nuanced variations in material behavior and ensuing device performance. The comprehensive particle size analysis serves as a cornerstone for unraveling the intrinsic relationships between growth kinetics, morphological attributes, and the consequential impact on material functionality.

Wettability investigations were meticulously conducted to elucidate the surface characteristics and wetting behavior of both the TiO2 and TiO2/AgBi2S3 composite thin films, each synthesized through varying SILAR cycle numbers (5, 10, and 15). The experimental setup employed a bespoke high-definition 16 megapixel Sony IMX 471 camera, facilitating precise shape and contact angle measurements of water droplets. Distilled water droplets of equal volumes were dispensed onto the pristine TiO2 and TiO2/AgBi2S3 composite thin films using a calibrated micropipette. High-resolution images of the water droplets on the film surfaces were captured using the aforementioned high-definition 16 megapixel Sony IMX 471 camera. Utilizing specialized software, the acquired images were subjected to advanced image analysis techniques. The software accurately determined the three-phase contact angle formed at the interface of the water droplet, film surface, and surrounding air. The contact angle was calculated as the angle between the tangent line drawn at the liquid-solid interface and the tangent line drawn at the liquid-vapor interface of the droplet. To ensure statistical rigor, multiple measurements of contact angles were conducted at distinct locations on each film sample. The resulting dataset was meticulously analyzed to ascertain the representative contact angle for each thin film type and SILAR cycle number. Prior to the experimentation, meticulous standardization and calibration procedures were employed to ensure accurate and consistent droplet dispensing, illumination, and imaging conditions. The calibration process involved the use of known reference liquids with established contact angle values. A comprehensive error analysis was conducted to gauge the measurement uncertainties associated with the contact angle determination. The uncertainties encompassed factors such as droplet size, camera calibration, and potential surface irregularities.

The recorded contact angle values, elaborated in Fig. 5, illuminate the nuanced wetting behavior across the film substrates. Upon examination of the TiO2 thin film, the distinctive protuberant shape of the water droplet is indicative of a moderate hydrophilic nature, with a corresponding contact angle range of approximately 330–340°. Remarkably, the introduction of AgBi2S3 nanoparticles onto the TiO2 surface precipitated a substantial alteration in the wetting characteristics. Evidently, the contact angle of the TiO2 thin film experienced a conspicuous reduction, ultimately settling within the range of 170–180° post- AgBi2S3 deposition. This transformative shift suggests a heightened wetting propensity, reflective of augmented surface energy and chemical interactions engendered by the presence of AgBi2S3 nanoparticles. Of particular interest is the constancy observed in contact angle values across all three SILAR cycle numbers (5, 10, and 15), as expounded in Fig. 5. This intriguing observation underscores the conclusion that the number of SILAR cycles yields a negligible influence on the wetting properties of the composite film. The unswerving nature of the contact angle values

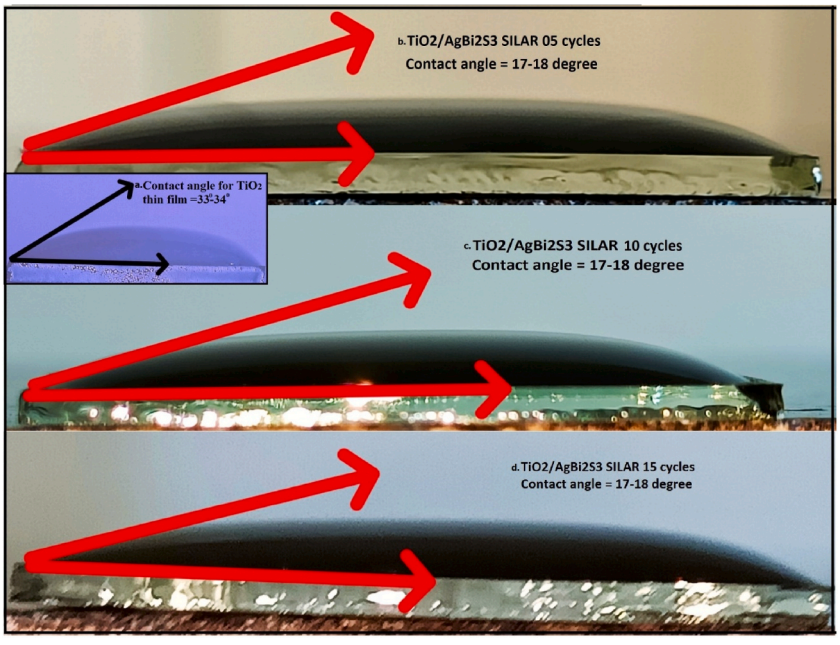

Fig. 5. Contact angle measurement for a) TiO_2 thin film around (33°-34°) & b-c-d) $TiO_2/AgBi_2S_3$ composite thin film around (17°-18°) for 5, 10 & 15 SILAR cycles respectively.

across varying deposition conditions underscores the inherent stability of the hydrophilic nature. This robust and consistent hydrophilic character holds critical implications for the material's utility. An augmented hydrophilic surface augments wetting behavior, thereby facilitating the effective penetration of electrolytes into the film. This, in turn, culminates in bolstered charge transfer processes, subsequently enhancing the performance metrics of the device. The augmented wetting behavior, coupled with improved electrolyte diffusion, collectively foster heightened device functionality. This encompasses a multitude of aspects, including heightened light absorption, enhanced charge extraction dynamics, and an overall amplification in device efficiency—a testament to the multifaceted advantages arising from a judicious manipulation of wetting behavior in thin film composites [25].

3.3. Elemental analysis

To ascertain the elemental constituents encapsulated within the synthesized TiO2/AgBi2S3 composite thin films, a meticulous investigation employing scanning electron microscopy (SEM) provided with energy dispersive X-ray spectroscopy (EDXS) attachment was undertaken. Diverse regions spanning each thin film, synthesized via 5, 10, and 15 SILAR cycles, were judiciously chosen for comprehensive elemental analysis, ensuring a representative examination of the film's composition. The resulting EDXS spectra lucidly manifest distinctive emission lines corresponding to the elemental signatures of Titanium(Ti), Oxygen(O), Silver(Ag), Bismuth (Bi), and Sulfur(S). This definitive elemental fingerprint corroborates and corroborates the earlier elucidated synthesis of the TiO2/

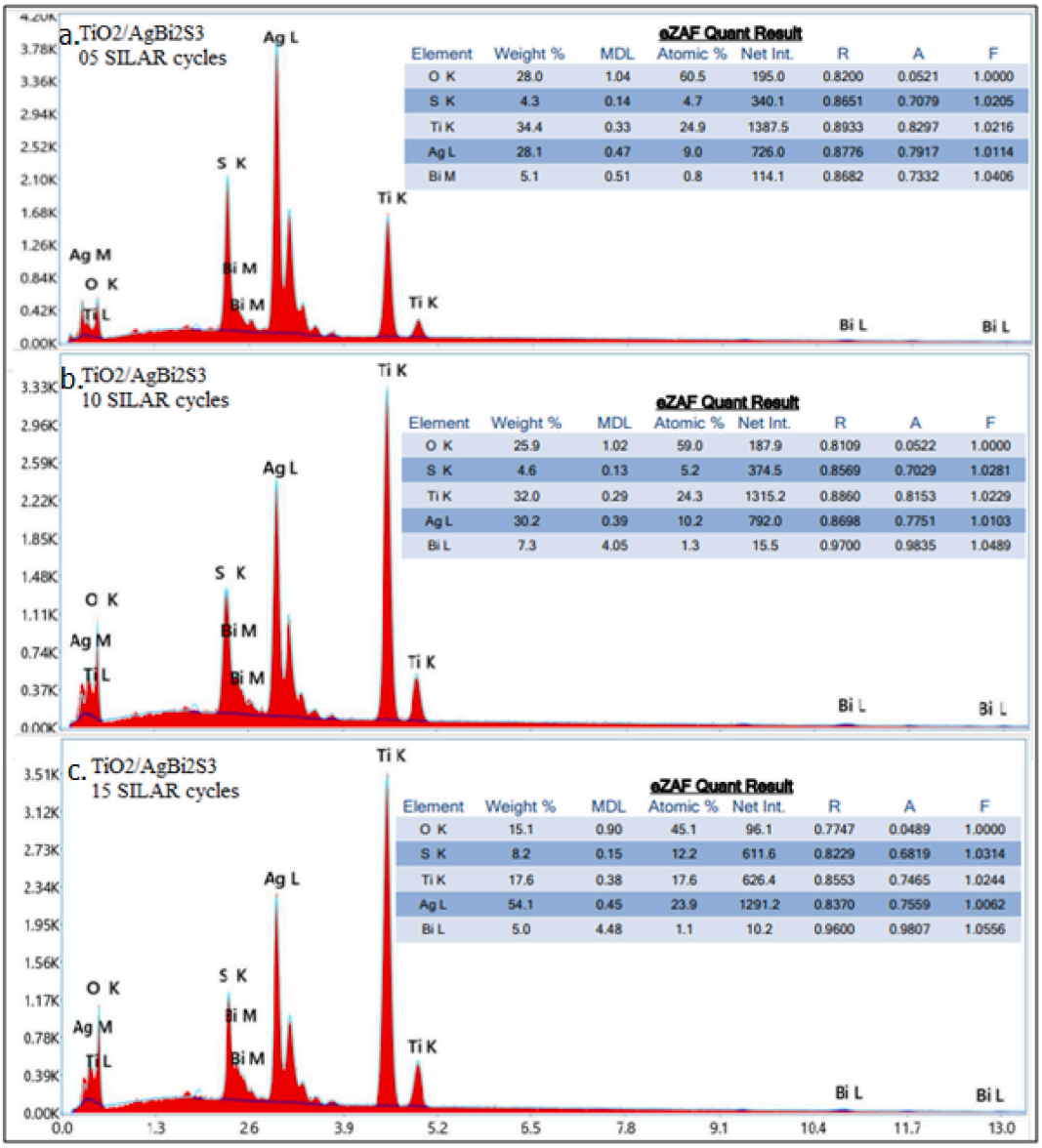

Fig. 6. EDXS spectrum for $TiO_2/AgBi_2S_3$ composite thin film for a) 5 b) 10 & c) 15 SILAR cyclesrespectively

AgBi2S3 composite thin film, as previously deduced from the comprehensive structural analysis facilitated by X-ray diffraction (XRD) techniques. The elemental distribution, quantified as weight percentages, unveils intriguing trends as the number of SILAR cycles advances from 5 to 15, as vividly depicted in Fig. 6. This observation encapsulates the underlying stability of the elemental composition vis-à-vis the deposition process, thus attesting to the judicious and consistent manipulation of synthesis conditions. Significantly, a discernible augmentation in the weight percentage of Silver (Ag) is discernible; signifying an amplified presence of Ag nanoparticles interwoven within the TiO2 matrix. This nuanced progression in the Ag percentage unequivocally implies that the number of SILAR cycles effectively governs the quantity of Ag nanoparticles seamlessly integrated into the TiO2 framework. This enhanced loading of Ag nanoparticles is indicative of a pronounced influence exerted by the SILAR cycle number on the quantity and spatial distribution of

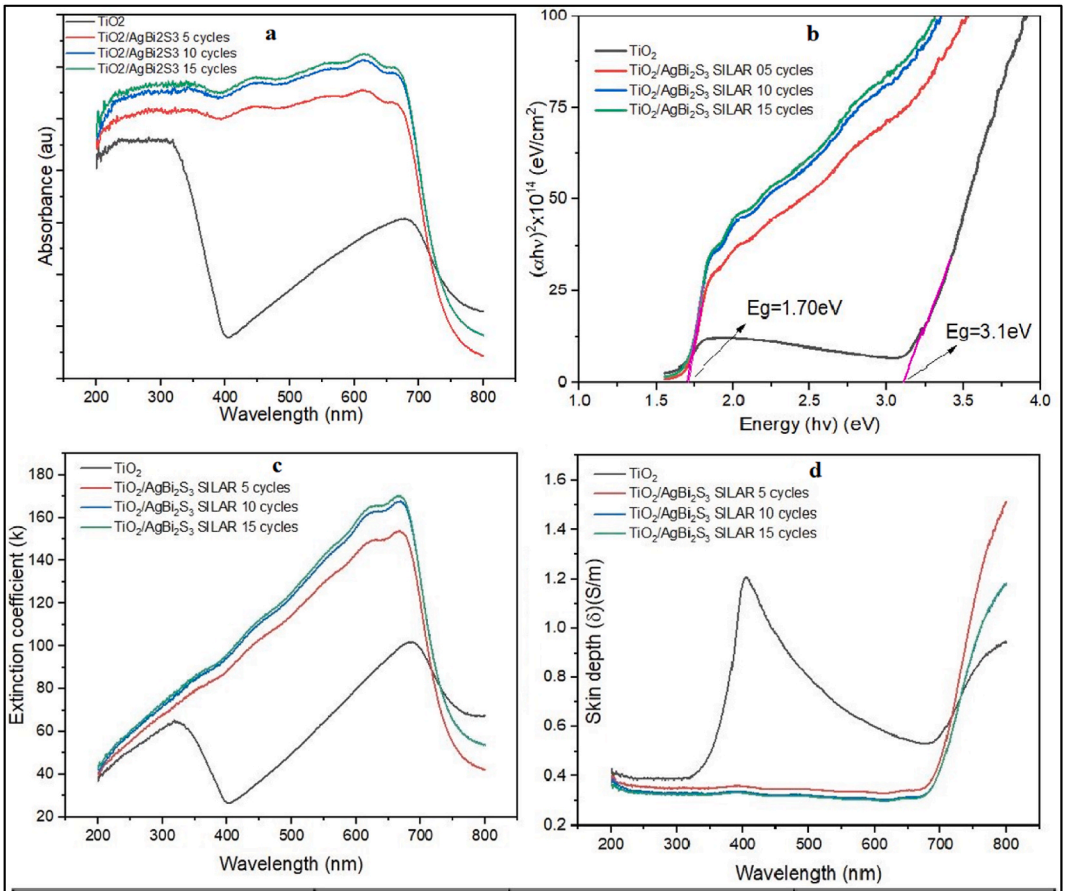

e

Thin film combination	Number of SILAR Cycles	Extinction Coefficient $K = \frac{\alpha \lambda}{4\pi}$	Skin depth (S/m) $\delta = \frac{1}{\alpha}$
TiO_2	Spin coating	62.347	0.669
$TiO_2/AgBi_2S_3$	05	95.890	0.468
$TiO_2/AgBi_2S_3$	10	104.185	0.418
$TiO_2/AgBi_2S_3$	15	105.763	0.413

Fig. 7. a) Absorbance b) Optical energy band gap (Eg) c) Variation in extinction coefficient (k) and d) skin depth (δ) as a function of wavelength incident light for TiO_2 thin film, $TiO_2/AgBi_2S_3$ composite thin film for 5, 10, 15 SILAR cycles & e) Summary of extinction coefficient (k) and skin depth (δ) for TiO_2 thin film, $TiO_2/AgBi_2S_3$ composite thin films.

Ag entities. AgNO3 is more reactive than Bi(NO3)3·5H2O due to the higher electronegativity of silver. This results in a stronger pull on the shared electrons in the covalent bond between the metal and the nitrate ion, making the silver-nitrate bond weaker and more susceptible to attack by other reactants. As a result, during the SILAR deposition process, silver nitrate is more likely to react with the TiO2 thin film than bismuth nitrate pentahydrate. This leads to a higher percentage of silver in the AgBi2S3 thin film as the number of SILAR cycles is increased. This augmentation, stemming from controlled deposition processes, bears paramount implications for the film's photoelectrochemical properties, offering a realm of enhanced functionality and potential applications.

In summation, the EDXS elemental analysis substantiates the profound influence of the deposition process, particularly the number of SILAR cycles, on the composite's elemental composition. This diligent assessment underscores the judicious synthesis conditions that orchestrate the harmonious integration of Ag and Bi2S3 nanoparticles within the TiO2 matrix, bestowing the resultant thin films with tailored and augmented material attributes. The systematic shifts in the elemental composition underscore the intricate interplay between deposition conditions and the resultant film architecture. The augmented presence of Ag nanoparticles, balanced against the nuanced variations in Ti, O, Bi, and S contents, accentuates the fine-tuned control achieved over the synthesis process. These findings collectively underscore the intricate correlations between SILAR cycle numbers and elemental composition, encapsulating the multidimensional facets of film synthesis and providing a foundation for optimizing material attributes tailored to specific applications.

3.4. Optical analysis

Fig. 7 (a) exhibits plot of absorbance as a function of wavelength of incident light (200 nm–800 nm) for TiO2 thin film and TiO2/AgBi2S3 composite thin film for 5, 10 & 15 SILAR cycles obtained from UV–Visible spectroscopy. With regard to TiO2 thin film the absorbance is optimum in the wavelength range 200 nm–325 nm. This suggests that the TiO2 thin film is particularly effective in harnessing energy from ultraviolet (UV) radiation. Beyond this range the absorbance of film depreciates sharply and attains minimal value at around 400 nm. Further the absorbance surge gradually and procure second maxima around 700 nm as noticed in Fig. 7 (a). This secondary maximum implies that the TiO2 film possesses additional absorption capabilities in the near-infrared (NIR) region. In the context of our research, it was observed that there exists a negative correlation between optical absorbance and the rotational deposition speed. Specifically, lower rotational speeds employed during the spin coating process were found to be associated with augmented film thickness, consequently yielding elevated levels of optical absorbance [26,27]. When AgBi2S3 thin film is embedded onto TiO2 thin film by SILAR technique there is appreciable change in optical absorbance of the thin film as shown in Fig. 7 (a). This enhancement in absorbance indicates improved light absorption capabilities of the composite film across a wide range of frequencies. All the three SILAR cycles (5, 10 & 15) exhibit almost identical plateau like absorbance curve as the function of frequency of incident light. This consistent behavior suggests that the SILAR process leads to reproducible and stable optical properties of the TiO2/AgBi2S3 composite film. Such consistency is crucial for practical applications and indicates the reliability of the fabrication process. Absorbance of TiO2/AgBi2S3 composite thin film shows elevation in entire visible region (400 nm–700 nm) as well as near infra red region (200 nm–400 nm) of the spectrum. This broadened absorbance range implies an expanded ability to capture and utilize light energy across a wider range of wavelengths. The broader absorbance spectrum enables the utilization of a larger portion of the solar spectrum. This behavior of composite film implies higher absorbance of incident light which would consequently have impact on its photo-electrochemical performance [28].

Fig. 7 (b) shows Tauc plot derived from absorbance spectrum for TiO2 thin film and TiO2/AgBi2S3 composite thin film for 5, 10 & 15 SILAR cycles [29]. The plot is useful tool in determining optical band gap energy of materials. The optical band gap energy of TiO2 thin film embedded by spin coating approach and annealed at 400 °C is computed equal to 3.1 eV which agrees with already established data. When this thin film of TiO2 is sensitized with AgBi2S3 thin film by SILAR technique (5, 10 & 15 cycles) the resulting optical band gap energy is reduced to 1.70 eV. The decrease in the band gap narrows the energy difference required for electron excitation, enabling the composite thin film to absorb photons with lower energies. This enhanced light absorption can be attributed to the synergistic effects of the TiO2 and AgBi2S3 components in the combined film. The tunable band gap of the composite thin film offers opportunities for tailoring its optical properties. The controlled deposition of the AgBi2S3 thin film onto the TiO2 surface allows for precise tuning of the composite film's band gap. This decrement in energy band gap value suggests plummeting of conduction band of TiO2 which can provide impelling force in charge segregation process at the junction [30].

Extinction coefficient (k) of thin film is the measure how the films absorbs incident light corresponding specific wavelength and skin depth (δ) of thin film is the measure of how far the incident light penetrates into it before getting significantly damped. Table illustrated in Fig. 7 (e) shows values of extinction coefficient (k) and skin depth (δ) for TiO2 thin film and TiO2/AgBi2S3 composite thin film for 5, 10 & 15 SILAR cycles. Equations (4) and (5) can be used to determine extinction coefficient (k) and skin depth (δ) of thin films [31,32],

$$k = \frac{\alpha\lambda}{4\pi} \tag{4}$$

$$\delta = \frac{1}{\alpha} \tag{5}$$

Where α is optical conductivity and λ is the wavelength of light incident. The surge in extinction coefficient and declining of skin depth in the table shown in Fig. 7 (e) indicates that the light wave is confined to the surface of the thin film which subsequently boost absorption of light as discussed in optical properties [33]. The value of extinction coefficient and skin depth for TiO2/AgBi2S3

composite thin film has marginally increased as number of SILAR cycles is increased as recorded in table depicted in Fig. 7 (e). Fig. 7(c and d) shows variation in extinction coefficient (k) and skin depth (δ) as a function of wavelength of incident light. For TiO2 thin film and TiO2/AgBi2S3 composite thin film the value of extinction coefficient is maximum around 650 nm–700 nm, which implies optimum light is absorbed in this wavelength range. Thus, film is becoming more opaque and transmitting minimal light through it. Same light absorbing behavior is reflected in skin depth plot. Value of skin depth is almost constant in the range 200 nm–700 nm beyond this there is surge. The uniformity in the skin depth in case of TiO2/AgBi2S3 composite thin film for all SILAR cycles indicates good light absorption of light in the specified wavelength range. Equivalent inference is drawn from absorbance plot as discussed in earlier section.

3.5. Electrochemical impedance spectroscopy analysis

Fig. 8 (a) shows electrochemical impedance spectroscopy analysis for FTO/TiO_2/polysulfide electrolyte/carbon electrode/FTO and FTO/TiO_2/$AgBi_2S_3$/polysulfide electrolyte/carbon electrode/FTO combination under dark condition for 5, 10 & 15 SILAR cycles. The strength of modulation signal with 5.0 mV ranging from 1.0 MHz to 0.10 Hz was applied to the combination. The Nyquist plot is represented by real part of impedance at X axis and its imaginary part at Y axis. For TiO_2 thin film the plot consists of only one semicircle at higher frequency which states higher charge transfer resistance & recombination resistance at the carbon electrode/polysulfide electrolyte interface [34]. In case of TiO_2/$AgBi_2S_3$ composite thin film as the number of SILAR cycles are increased the size of first semicircle at higher frequencies is reduced which implies lowering of charge transfer resistance at carbon electrode/polysulfide electrolyte interface as seen in Fig. 8 (a) [35]. The lower resistance facilitates more efficient electron transfer between the electrode and the electrolyte, leading to improved charge transport and overall device performance. As the SILAR cycles increases, the composite thin film undergoes changes in its morphology, such as increased particle size or improved interparticle connectivity. This may further result in better photovoltaic performance. But as the SILAR cycles are increased the diameter of second semi circle amplifies indicating rise in charge transfer resistance at $AgBi_2S_3$/polysulphide electrolyte interface. As the number of cycles increases, the $AgBi_2S_3$ thin film may undergo structural modifications such as increased particle size, reduced surface area, or alterations in the interfacial characteristics. These morphological changes can affect the kinetics of charge transfer and lead to the observed rise in resistance. There can be

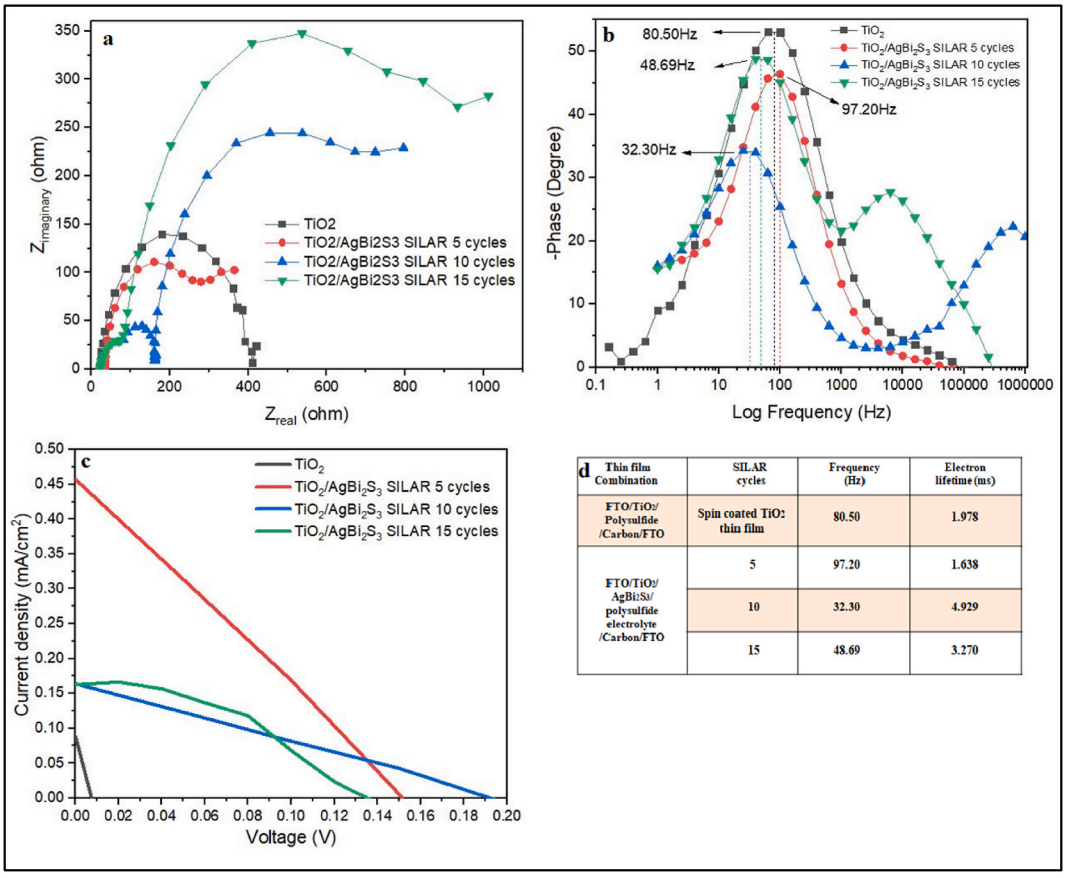

Thin film Combination	SILAR cycles	Frequency (Hz)	Electron lifetime (ms)
FTO/TiO2/ Polysulfide /Carbon/FTO	Spin coated TiO2 thin film	80.50	1.978
FTO/TiO2/ AgBi2S3/ polysulfide electrolyte /Carbon/FTO	5	97.20	1.638
	10	32.30	4.929
	15	48.69	3.270

Fig. 8. a) Nyquist plot b) Bode plot c) Photoelectrochemical performance & d) Electron lifetime for TiO_2 thin film and TiO_2/$AgBi_2S_3$ composite thin film device for 5, 10 & 15 SILAR cycles with polysulfide electrolyte.

many reasons for this rise such as imperfect contact between $AgBi_2S_3$ and polysulphide electrolyte, inefficient dye generation or decreased electron mobility in the TiO_2 thin film [36].

Fig. 8 (b) represent Bode phase plot for TiO2 thin film and TiO2/AgBi2S3 composite thin film for SILAR 5, 10 & 15 cycles with FTO/TiO2/AgBi2S3/polysulfide electrolyte/carbon electrode/FTO combination. The frequency axis varies from 1 Hz to 1 MHz and phase axis varies from 00 to 500 as shown in Fig. 8 (b). The high gradient slope of the all curves in Bode plot implies clumsy charge transfer between AgBi2S3 and TiO2 electrode at low frequencies. The peaks of the curves can be utilized to estimate electron lifetime using equation (6) [37].

$$\tau = \frac{1}{2\pi f} \tag{6}$$

Here τ is electron lifetime & f is maximum frequency from Bode plot as shown in Fig. 8 (b). Lifetime of electron is optimum for 10 SILAR cycles as indicated in table shown in Fig. 8 (d). The first peak in the Bode plot is the resonant frequency for the electrical circuit of the fabricated combination and the second peak in the case of 10 & 15 SILAR cycles can be for resonant frequency for dye molecules [38] i; e $AgBi_2S_3$.

3.6. Photoelectrochemical analysis

The photoelectrochemical analysis of the device fabricated FTO/TiO_2/polysulfide electrolyte/carbon electrode/FTO and FTO/TiO_2/$AgBi_2S_3$/polysulfide electrolyte/carbon electrode/FTO combination is shown in Fig. 8 (c). The polysulfide electrolyte was prepared using 1 M of sulfur powder, sodium hydroxide (NaOH) and sodium sulfide (Na_2S) mixed together in 8 ml of ethanol and 2 ml of distilled water. This solution was stirred for 10 min and later filtered to remove any undissolved solid material. The electrolyte obtained is transparent yellow colored liquid. The device was fabricated with counter electrode made up of carbon suit deposited on FTO. Few drops of polysulfide electrolyte were released between the sandwiched patterns of FTO/TiO_2/$AgBi_2S_3$/polysulfide electrolyte/carbon electrode/FTO combination and then it was tested for photoelectrochemical performance. The plot of current density as the function of applied voltage for TiO_2 thin film and TiO_2/$AgBi_2S_3$ composite thin film for SILAR 5, 10 & 15 cycles is shown in Fig. 8 (c). The JV plot shows optimum performance for 5 SILAR cycles with maximum short circuit current of 0.2854 mA/cm^2. Later the photovoltaic performance is reduced. The summary of photoelectrochemical performance is represented in Table 1.

4. Conclusions

In this study successfully demonstrates the facile synthesis of AgBi2S3 thin films onto TiO2 substrates via the SILAR technique employing varying cycle numbers (5, 10, and 15). The versatility of SILAR as a straight forward deposition approach for diverse thin film materials is highlighted. Tailoring the properties of the deposited films is achievable by modulating precursor molarity, immersion time, and temperature. XRD analysis unequivocally confirms the polycrystalline nature of AgBi2S3 films atop anatase TiO2 substrates. SEM elucidates the spherical morphology of the nanoparticles and reveals a thickness evolution proportional to SILAR cycles. The hydrophilic propensity of the TiO2 thin film is distinctly augmented upon AgBi2S3 deposition, underscoring interfacial alterations. Elemental analysis by EDXS corroborates the successful integration of AgBi2S3 onto the TiO2 matrix. UV–Visible absorbance spectra of

Table 1
Photoelectrochemical performance of TiO_2 thin film and TiO_2/$AgBi_2S_3$ composite thin film device for SILAR 5, 10 & 15 cycles with polysulfide electrolyte.

Sr No	Device	SILAR cycles	Sun	Area (cm^2)	I_{sc} mA	V_{oc} V	Pmax mW	I_{max} mA	V_{max} V	Efficiency	Fill factor	J_{sc} mA/cm^2
1	FTO/TiO_2/ polysulfide electrolyte/ carbon-electrode /FTO	Spin coated	1	0.5	0.0442	0.0074	——	0.0442	——	——	——	0.0884
2	FTO/TiO_2/ $AgBi_2S_3$ /polysulfide electrolyte/ carbon-electrode /FTO	5	1	0.5	0.2854	0.1514	0.0084	0.0843	0.1	0.0168	24.36	0.4570
3		10	1	1	0.1628	0.1354	0.0094	0.1180	0.08	0.0094	42.82	0.1628
4		15	1	1.5	0.2457	0.1924	0.0122	0.1221	0.1	0.0081	25.83	0.1638

the TiO2/AgBi2S3 composite manifest heightened light absorption, while a noteworthy reduction in the optical energy band gap from 3.10 eV to 1.70 eV is observed. EIS investigations reveal varying charge transfer resistances at different interfaces, influencing the photoelectrochemical performance of the device. In summation, the exceptional light-absorbing capabilities, favorable optical properties, and non-toxic nature of AgBi2S3 make it a compelling candidate for further exploration in optoelectronic applications. Future research endeavors will be directed towards advancing the understanding of AgBi2S3 -based systems for enhanced optoelectronic functionalities.

Funding

The authors did not receive support from any organization for the submitted work.

Data availability statement

The data that support the findings of this study are available from the corresponding author, [SAP], upon reasonable request.

Ethical approval

Not applicable

Additional information

No additional information is available for this paper.

CRediT authorship contribution statement

Sachin Padwal: Writing – review & editing, Writing – original draft, Visualization, Validation, Software, Resources, Methodology, Investigation, Formal analysis, Data curation, Conceptualization. **Rahul Wagh:** Writing – review & editing, Supervision, Software, Methodology, Conceptualization. **Jivan Thakare:** Supervision, Methodology, Formal analysis, Conceptualization. **Rajendra Patil:** Supervision, Methodology, Conceptualization.

Declaration of generative AI and AI-assisted technologies in the writing process

During the preparation of this work the author(s) used [CHATGPT TOOL] in order to [IMPROVE ENGLISH ONLY]. After using this tool/service, the author(s) reviewed and edited the content as needed and take(s) full responsibility for the content of the publication.

Declaration of competing interest

The authors have no conflict of interest to declare. Also, the authors have no known competing financial interests or personal relationship that could have appeared to influence the work reported in this paper.

Acknowledgment

The authors sincerely acknowledge the Kaviyatri Bahinabai Chaudhari North Maharashtra University Jalgaon, Department of Physics PSGVP Mandal's Arts, Commerce & Science College Shahada, Nandurbar, Advanced Physics Lab-Department of Physics, Savitribai Phule University Pune, Baburaoji Gholap Science College Pune and Icon Analytical New Mumbai for providing characterization facilities.

References

[1] IEA, World Energy Outlook, IEA, Paris, 2021. Available at: https://www.iea.org/reports/world-energy-outlook-2021. (Accessed 20 April 2023).
[2] IEA, Methane Tracker, IEA, Paris, 2023. Available at: https://www.iea.org/data-and-statistics/data-tools/methane-. (Accessed 20 April 2023).
[3] IEA, Global Energy Review, IEA, Paris, 2021. Available at: https://www.iea.org/reports/global-energy-review-2021;. (Accessed 20 April 2023).
[4] IEA, Solar Energy: Mapping the Road Ahead, IEA, Paris, 2019. Available at: https://www.iea.org/reports/solar-energy-. (Accessed 20 April 2023).
[5] L. Frass, L. Partain, Solar Cells and Their Applications, second ed., John Wiley & Sons Inc., NJ, USA, 2010.
[6] B. O'Regan, M. Gratzel, Nature 353 (1991) 737.
[7] J. Poortmans, V. Arkhipov, Thin film solar cells: fabrication, characterization, and applications, in: Wiley Series in Materials for Electronic & Optoelectronic Applications, Springer Science, Business Media, LLC, 2006.
[8] N.G. Park, K.M. Kim, M.G. Kang, K.S. Ryu, S.H. Chang, Y.J. Shin, Adv. Mater. 17 (2005) 2349.
[9] J.E. Ikpesu, S.E. Iyuke, M. Daramola, A.O. Okewale, Sol. Energy 206 (2020) 918.
[10] R.S. Mane, C.D. Lokhande, Mater. Chem. Phys. 65 (2000) 1.
[11] Y. Jia, R. Xu, K. Xu, S. Wang, X. Ren, N. Zhang, D. Wu, H. Ma, Y. Li, Q. Wei, Anal. Chem. 94 (33) (2023), 11713.
[12] P. Ganguly, S. Mathew, L. Clarizia, R.S. Kumar, A. Akande, S.J. Hinder, S.C. Pillai, ACS Omega 5 (1) (2020) 406.
[13] P.C. Huang, W.C. Yang, M.W. Lee, J. Phys. Chem. 26 (2013) 48.
[14] S. Zhou, J. Yang, W. Li, Q. Jiang, Y. Luo, D. Zhang, Z. Zhou, X. Li, J. Electrochem. Soc. 163 (3) (2016) D63.

[15] E. Gu, X. Lin, X. Tang, G.J. Matt, A. Osvet, Y. Hou, S. Jäger, C. Xie, A. Karl, R. Hock, C.J. Brabec, J. Mater. Chem. C 6 (2018) 7642.
[16] A.N. Rodriguez, M.T.S. Nair, P.K. Nair, Mater. Res. Soc. Symp. Proc. 730 (2002) V5.14.
[17] B. Pejova, I. Grozdanov, D. Nesheva, A. Petrova, Chem. Mater. 20 (7) (2008) 2551.
[18] N. Pai, J. Lu, D.C. Senevirathna, A.S.R. Chesman, T. Gengenbach, M. Chatti, A.N. Simonov, J. Mater. Chem. C 6 (10) (2018) 2483.
[19] Y. Cao, M. Bernechea, A. Maclachlan, V. Zardetto, M. Creatore, S.A. Haque, G. Konstantatos, Chem. Mater. 27 (10) (2015) 3700.
[20] B.D. Cullity, Elements of X-Ray Diffraction, second ed., Addison- Wesley Publishing Company, Inc., USA, 1978.
[21] X. Li, Y. Chen, L. Li, J. Huang, Mater 11 (9) (2018) 1759.
[22] V. Kaltenhauser, T. Rath, W. Haas, A. Torvisco, J. Mater. Chem. C 1 (2013) 7825.
[23] M.A. Islam, M.S. Hossain, M.M. Aliyu, P. Chelvanathan, Q. Huda, M.R. Karim, N. Amin, Energy Proc. 33 (2013) 203.
[24] Y. Tachibana, J.E. Moser, M. Gratzel, D.R. Klug, J.R. Durran, J. Phys. Chem. 100 (51) (1996), 20056.
[25] Chao Han, Chu Cheng, Fengling Liu, Xinli Li, Guangxin Wang, Jiwen Li, Nanotechnol. Rev. 12 (1) (2023), 20220503.
[26] Xinli Li, Kunjie Wang, Zhiping Mao, Joshi Mahesh Kumar, Chao Han, Lihua Li, Renhong Yu, Yongjun Gu, Yong Zhang.Vacuum 2023,217, 112579.
[27] X. Li, M. Yang, D. Zhu, L. Li, Z. Ma, X. Ning, B.H. Kim, J. Electron. Mater. 49 (2020) 3242.
[28] J. Liu, S. Li, J. Li, L. Zhang, Y. Li, Y. Wang, J. Mater. Sci. Mater. Electron. 26 (11) (2015) 8766.
[29] Y. Oner, I. Polat, S. Korkmaz, J. Mater. Sci. Mater. Electron. 29 (14) (2018), 11720.
[30] A. Kaniyoor, S. Ramaprabhu, P.K. Maiti, J. Phys. Chem. C 112 (12) (2008) 4653.
[31] K.R. Nemade, Russ. J. Non-Ferrous Metals 58 (1) (2017) 82.
[32] A. Abu El Hiaja, J. Optica Applicata 31 (4) (2001) 739.
[33] M. Alqatari, A.A. Alrashed, Sol. Energy 199 (2020) 32.
[34] A.J. Bard, L.R. Faulkner, Electrochemical Methods: Fundamentals and Applications, John Wiley & Sons, USA, 2001.
[35] J.R. MacDonald, Impedance spectroscopy, Ann. Biomed. Eng. 15 (5) (1987) 297.
[36] J. Wang, J. Li, P. Wang, J. Mater. Chem. A 1 (41) (2013), 13033.
[37] S. Majumder, Electrochim. Acta 222 (2016) 100.
[38] K. Kakiage, Y. Aoyama, T. Yano, K. Oya, J.I. Fujisawa, M. Hanaya, Chem. Commun. 51 (82) (2015), 14894.